Supporting Information

Copper-substituted incorporation for polytypism and bandgap engineering of $MAPbBr_3$ Perovskite thin films with enhanced Near-Infrared photocurrent-response

Amr Elattar,*[a,b] Jiban Kangsabanik,[c] Kodai Nakao,[a] Kosei Tsutsumi,[a] Hiroo Suzuki,[a] Takeshi Nishikawa,[a] Kristian S. Thygesen,[c] and Yasuhiko Hayashi[a]

Point defect simulation:

The formation energy of a defect D at a charge state 'q' can be expressed as follows,

$$E_{form}[D^q] = E_{tot}[D^q] - E_{tot}[pristine] - \sum n_i\mu_i + q(E_{VBM} + \Delta E_F) \ (1)$$

Here, $E_{tot}[D^q]$ is the total energy for a supercell associated with the aforementioned defect D. $E_{tot}[pristine]$ is the total energy of ther equivalent pristine bulk supercell. μ_i is the chemical potential of the associated defect with n_i being the number of defects added (n_i > 0) to or removed (n_i < 0) from the system. The next term accounts for the chemical potential of electrons added (q < 0) to or removed (q > 0) from the simulation box while creating various charged defect states. E_{VBM} is the energy of the valence band maxima. ΔE_F is the Fermi level position, which can be varied from zero (at VBM) to the bandgap (E_g) value (at CBM). In the following section, we discuss the choice of defects and the choice of chemical potentials (chemical growth conditions) for the constituents.

The charge transition levels (CTLs) are calculated by applying the Slater-Janak transition state theory[1], which assumes that Kohn-Sham eigenvalues are linearly dependent on the orbital occupation numbers. This method can be seen as an alternative to the correction schemes usually applied for charged defects and has been successfully used to predict the CTLs of various compounds (further details of this method can be found elsewhere[2,3]).

In this study, we consider Cu_{Pb}, v_{Br}, and MA_i individual point defects as well as Cu_{Pb}+v_{Br}, Cu_{Pb}+MA_i defect complexes. We see from eqn. 1 that the defect formation energies vary with μ. Experimentally, this chemical potential can vary depending on the growth environment. That is, if a growth environment is anion/cation poor (rich), creating anion/cation vacancies will be easy (difficult) and the opposite is true in the case of interstitials. Applying this basic understanding to eqn.(1) reveals to us that for an element A, $\mu_A^{poor} < \mu_A^{rich}$. The choice of chemical potentials for the constituent elements involved in Cu doping of $MAPbBr_3$ is therefore quite important.

The choice of μ generally depends on the stability of the compound against possible elemental and competing secondary phases. As such, the following thermodynamic (in) equations must be satisfied,

$$\Delta\mu_{MA} + \Delta\mu_{Pb} + 3\Delta\mu_{Br} = \Delta H_{f(\mathrm{MAPbBr_3})} \quad (2)$$

Here, ΔH_f is the formation enthalpy of $\mathrm{MAPbBr_3}$ against its elemental constituents.

Here, $\Delta\mu_A = \mu_A - \mu_A^0$, where μ_A^0 is the total energy of constituent 'A' in its elemental phase. To avoid co-existence of elemental and secondary phases, the following set of equations should also be satisfied,

$$\Delta\mu_A < 0, \ \mathrm{A=MA,\ Pb,\ Br} \quad (3)$$

$$p\Delta\mu_{MA} + q\Delta\mu_{Pb} + r\Delta\mu_{Br} < \Delta H_{f(\mathrm{MA_pPb_qBr_r})};\ p, q, r = 0, 1, 2 \ldots Z \quad (4)$$

Here, as secondary phases we have considered the following compounds: MA, Pb, Br, MABr, and $\mathrm{PbBr_2}$. We have chosen two possible scenarios namely- a) Pb rich/ Br poor and b) Pb poor / Br rich, and the corresponding chemical potential values of Cu are taken as $\Delta\mu_{Cu} = 0$ (Cu elemental phase) and $\Delta\mu_{Cu}$ = ($\Delta H_f(\mathrm{CuBr_2})$ -2$\Delta\mu_{Br}$). The chemical potential values are tabulated below.

Table S1. Chemical potential values for constituent elements associated with different growth conditions.

Condition	Pb rich / Br poor	Pb poor/ Br rich
$\Delta\mu_{MA}$	-2.1701 eV	-3.5609 eV
$\Delta\mu_{Pb}$	0 eV	-2.7816 eV
$\Delta\mu_{Br}$	-1.3908 eV	0 eV
$\Delta\mu_{Cu}$	0 eV	-0.994 eV

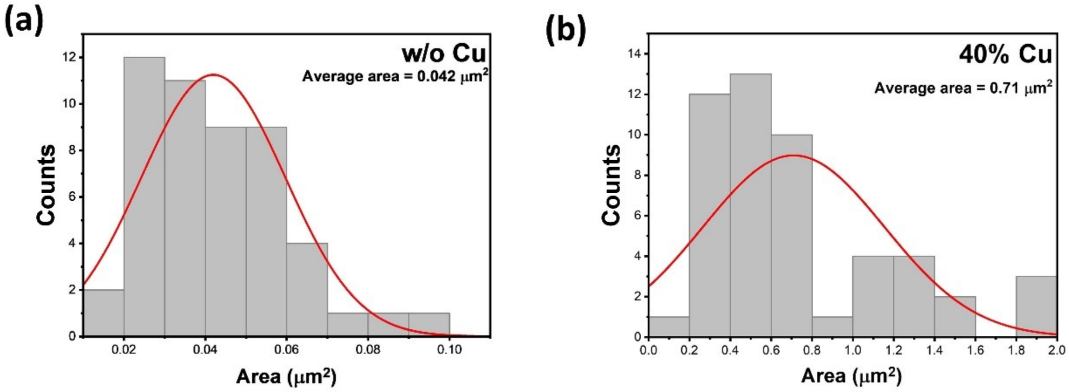

Fig. S1 Grain size distribution of (a) Pristine MAPbBr$_3$ thin film and (b) 40% Cu-doped MAPbBr$_3$ thin film.

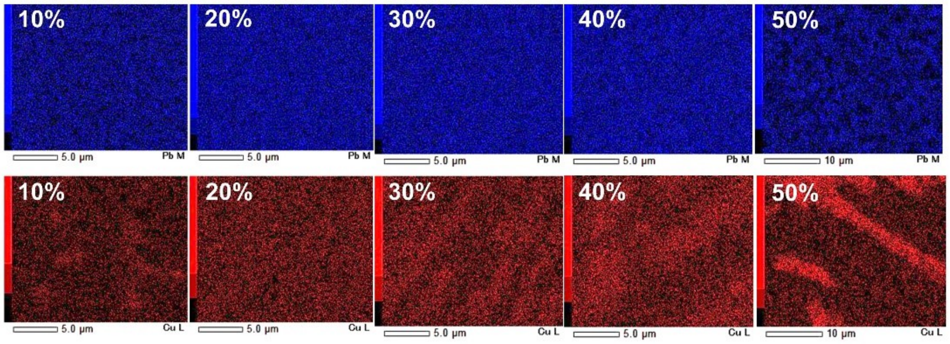

Fig. S2 EDS elemental mapping of Cu-doped MAPbBr$_3$ thin films: Pb(Blue) and Cu (Red).

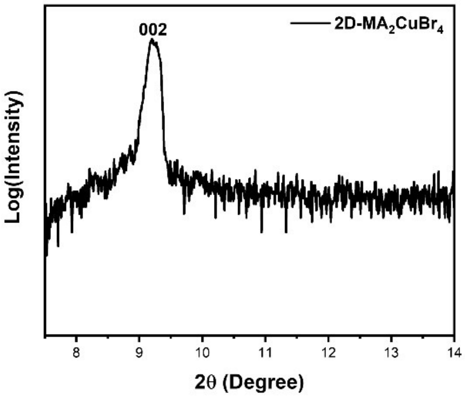

Fig. S3 XRD pattern (log scale) for the (002) peak of MA$_2$CuBr$_4$ perovskite at $2\theta = 9.2°$.

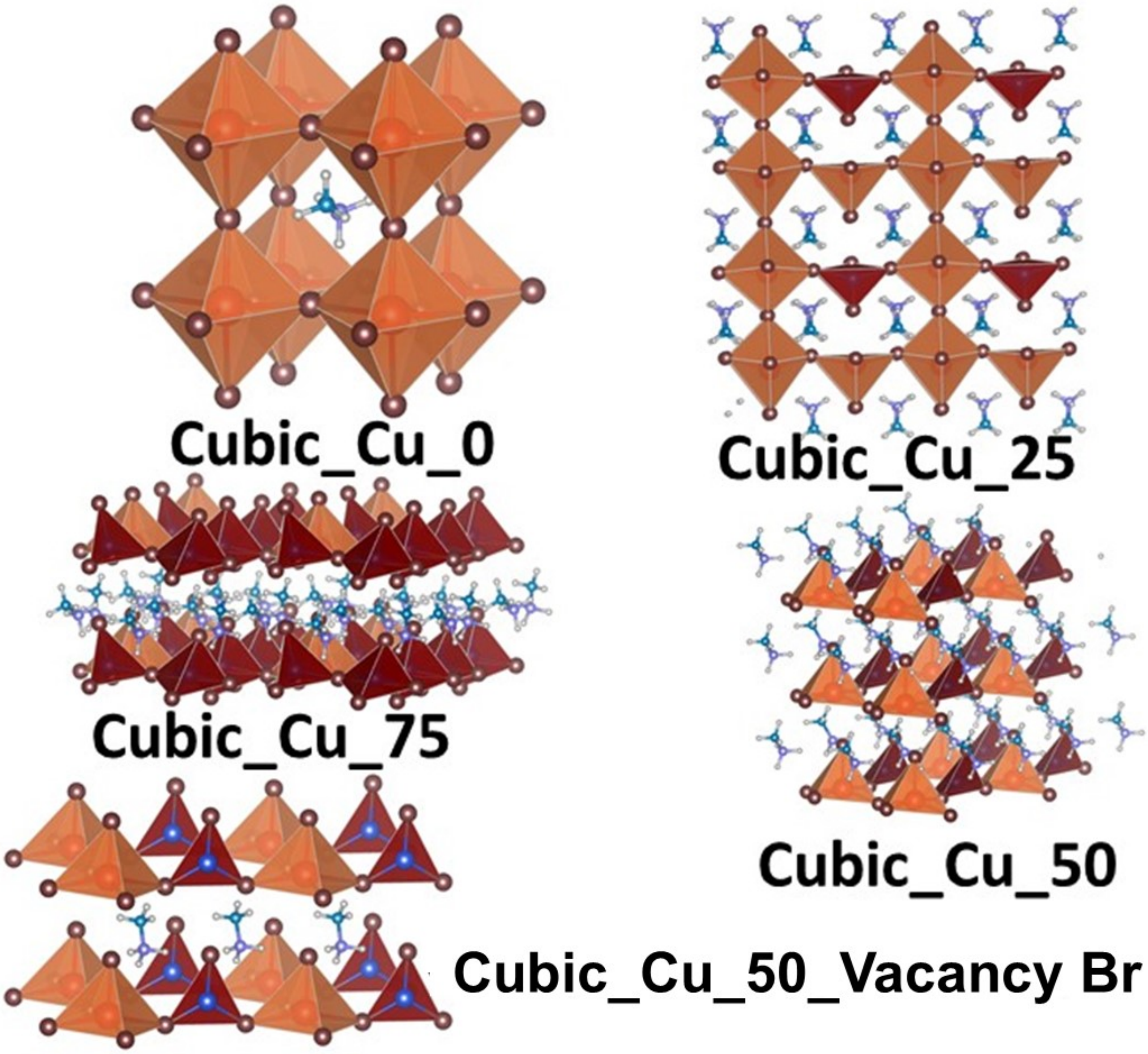

Fig. S4 Possible cubic crystal structures of 0, 25%, 50%, 75%, and 50% (with Br-vacancy) Cu-doped $MAPbBr_3$ perovskites.

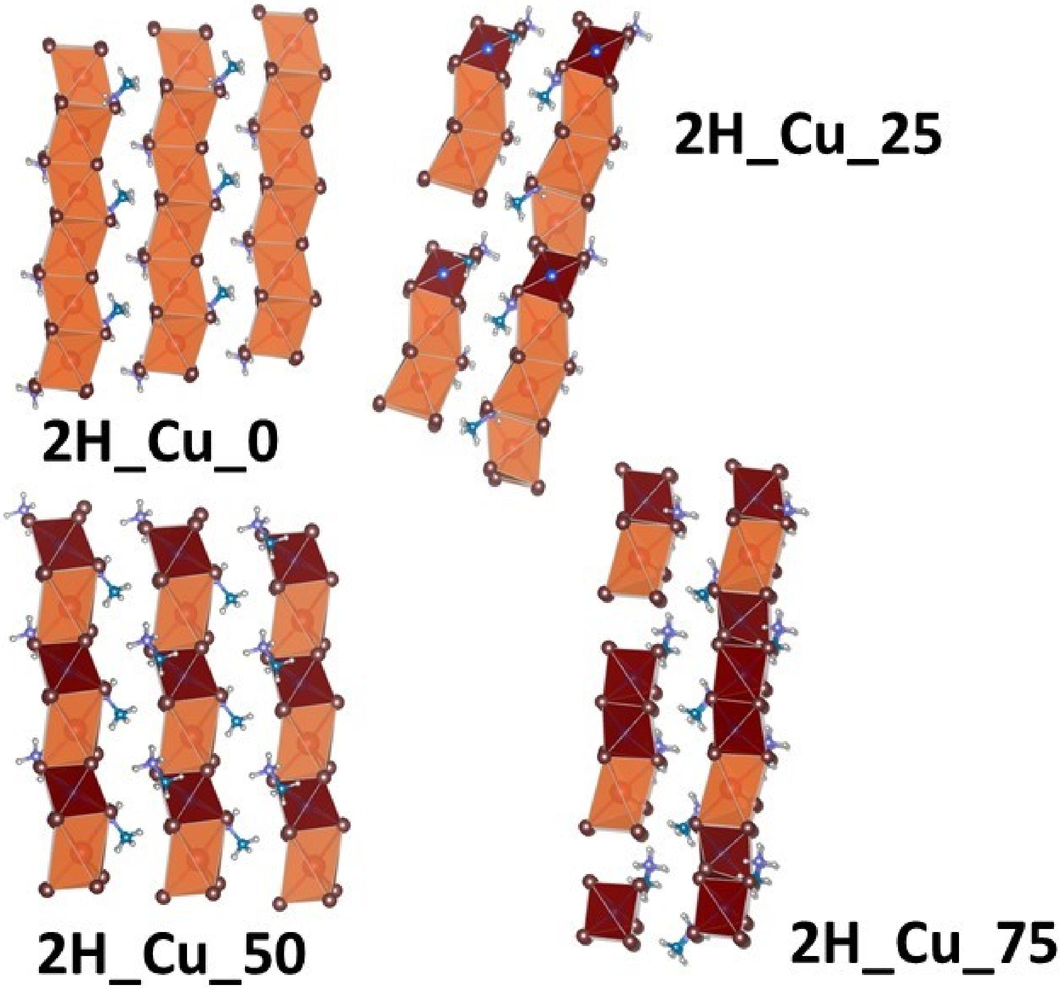

Fig. S5 Possible hexagonal (2H) crystal structures of 0, 25%, 50%, and 75% Cu-doped $MAPbBr_3$ perovskites.

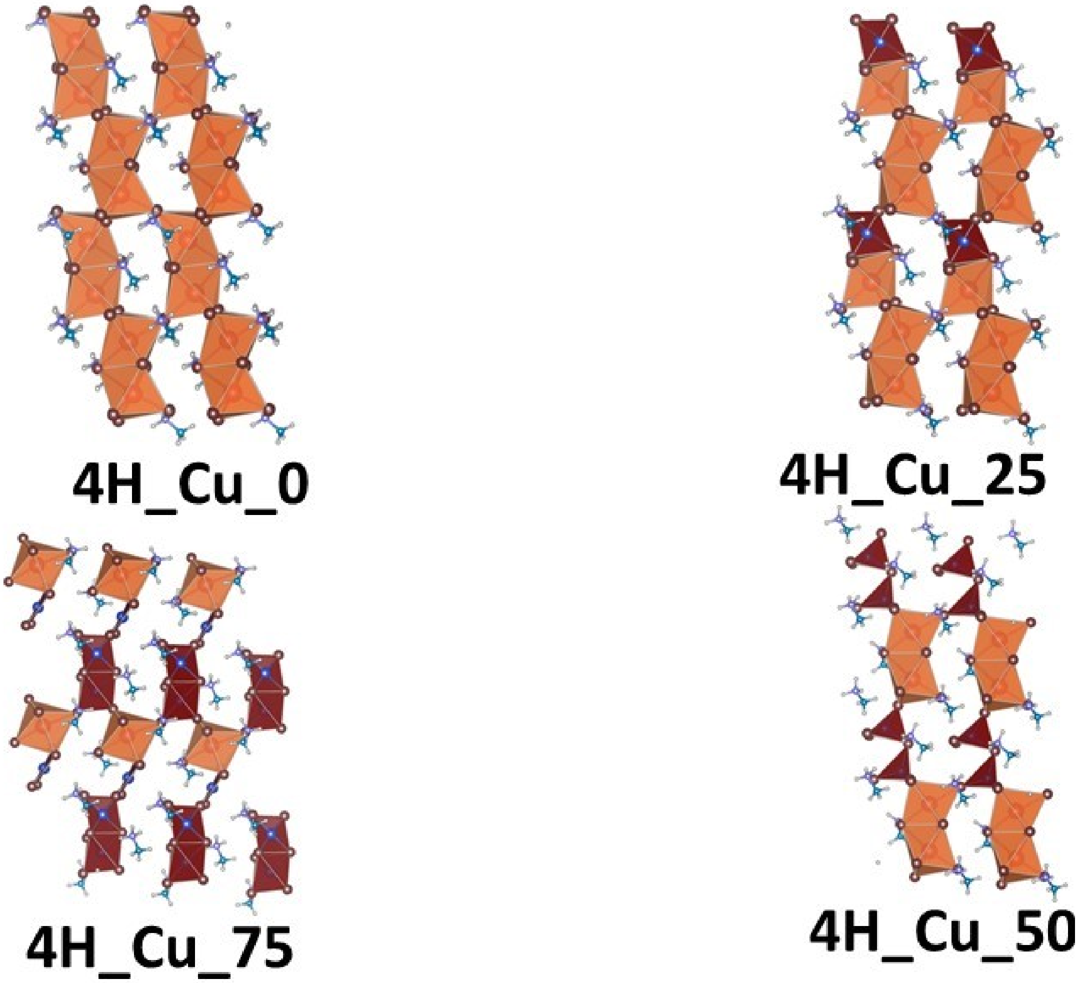

Fig. S6 Possible hexagonal (4H) crystal structures of 0, 25%, 50%, and 75% Cu-doped $MAPbBr_3$ perovskites.

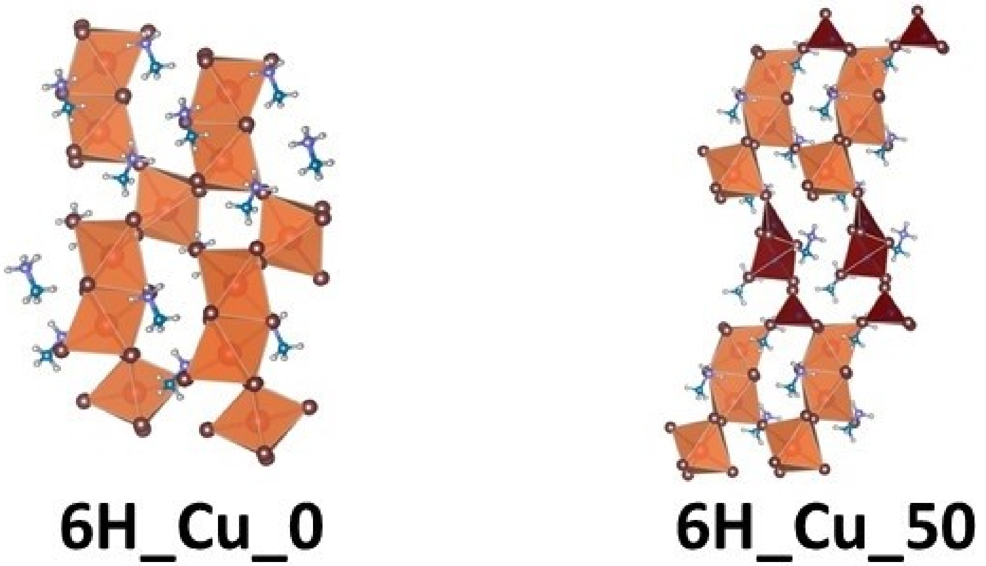

Fig. S7 Possible hexagonal (6H) crystal structures of 0 and 50% Cu-doped $MAPbBr_3$ perovskites.

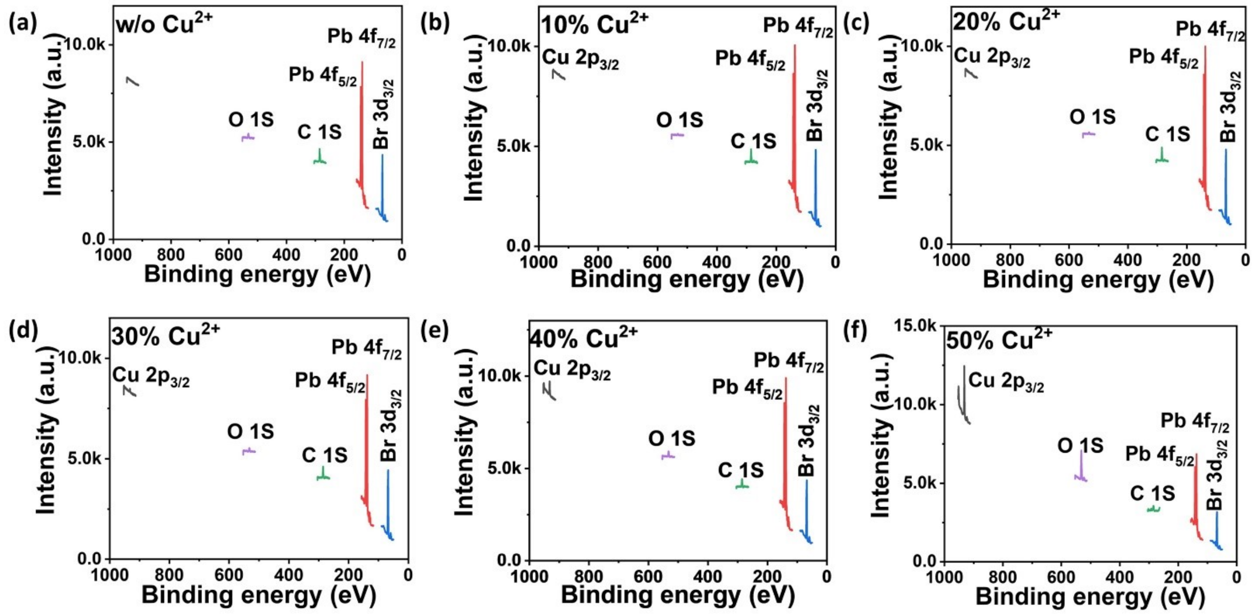

Fig. S8 XPS full spectra of Cu-alloyed $MAPbBr_3$ perovskites.

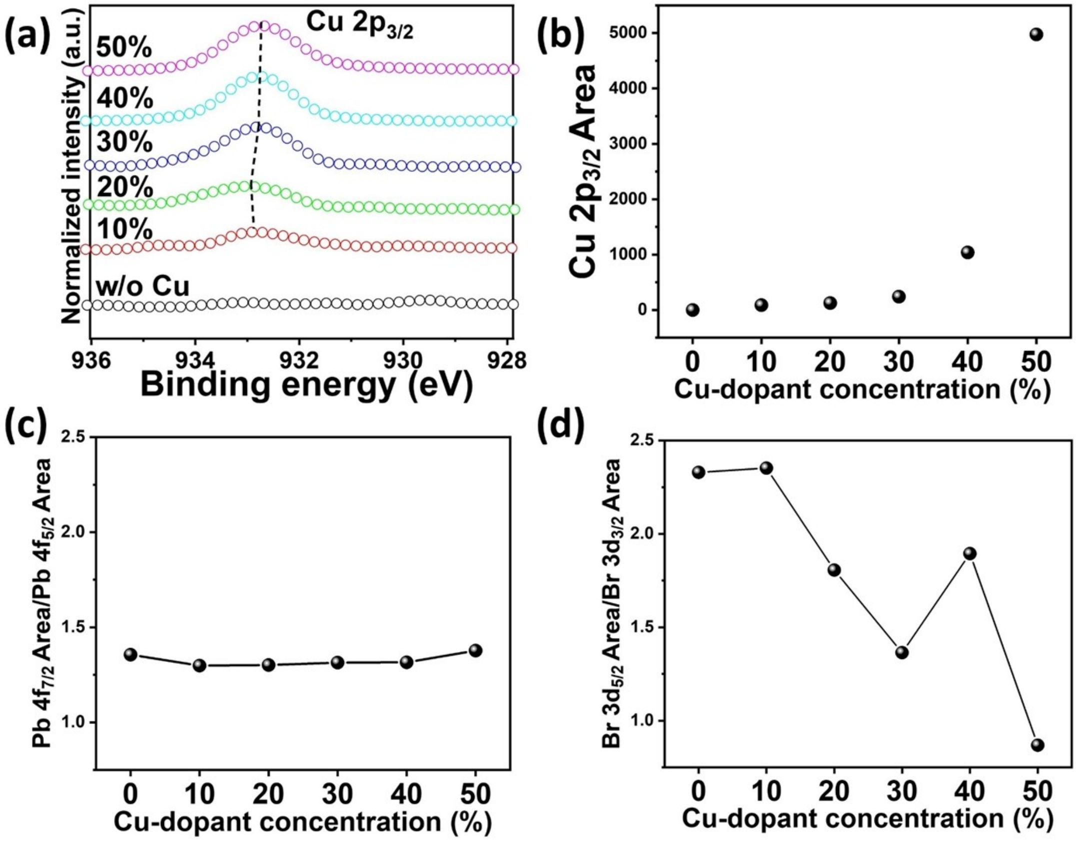

Fig. S9 (a) Normalized XPS spectra of Cu2p$_{3/2}$. XPS peaks area of Cu2p (b), Pb4f (c), and Br3d (d).

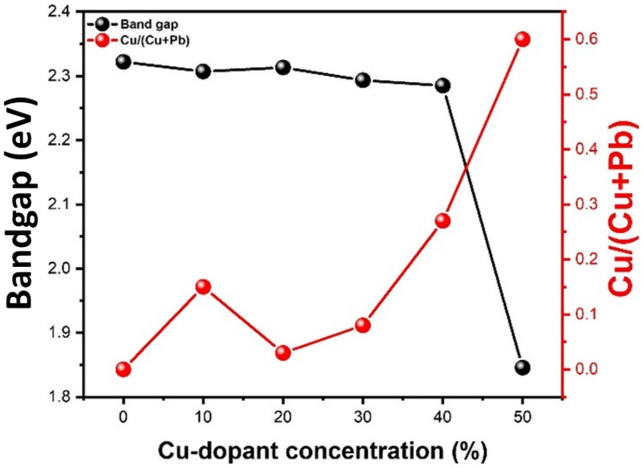

Fig. S10 Optical bandgap (obtained from absorption spectra) and Cu atomic% (obtained from EDS) as a function of Cu-dopant concentration.

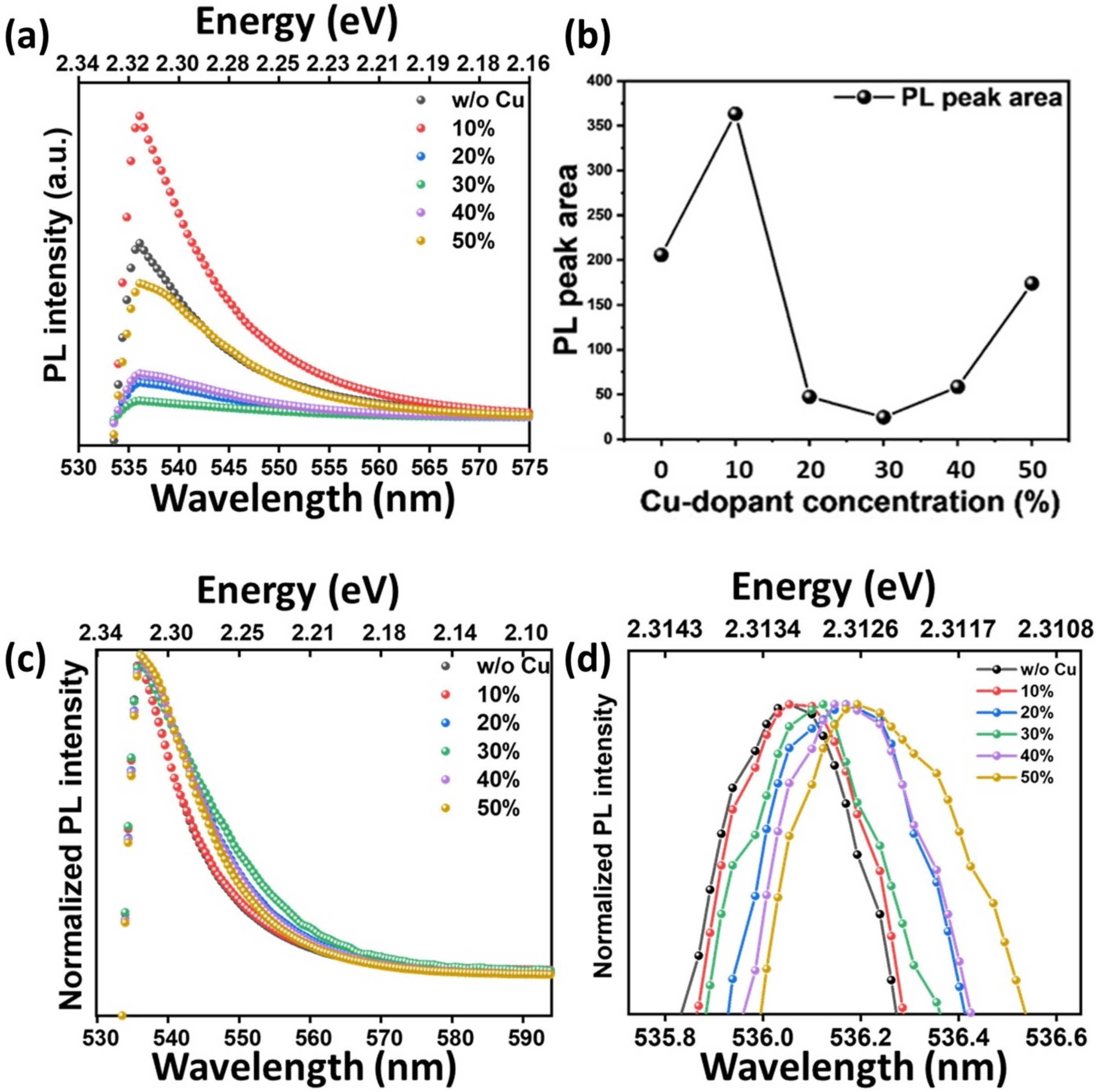

Fig. S11 Room temperature PL spectra (a), PL peak area (b), normalized PL spectra (c), and enlarged image of normalized PL spectra (d) for different Cu-dopant $MAPbBr_3$ perovskite thin films.

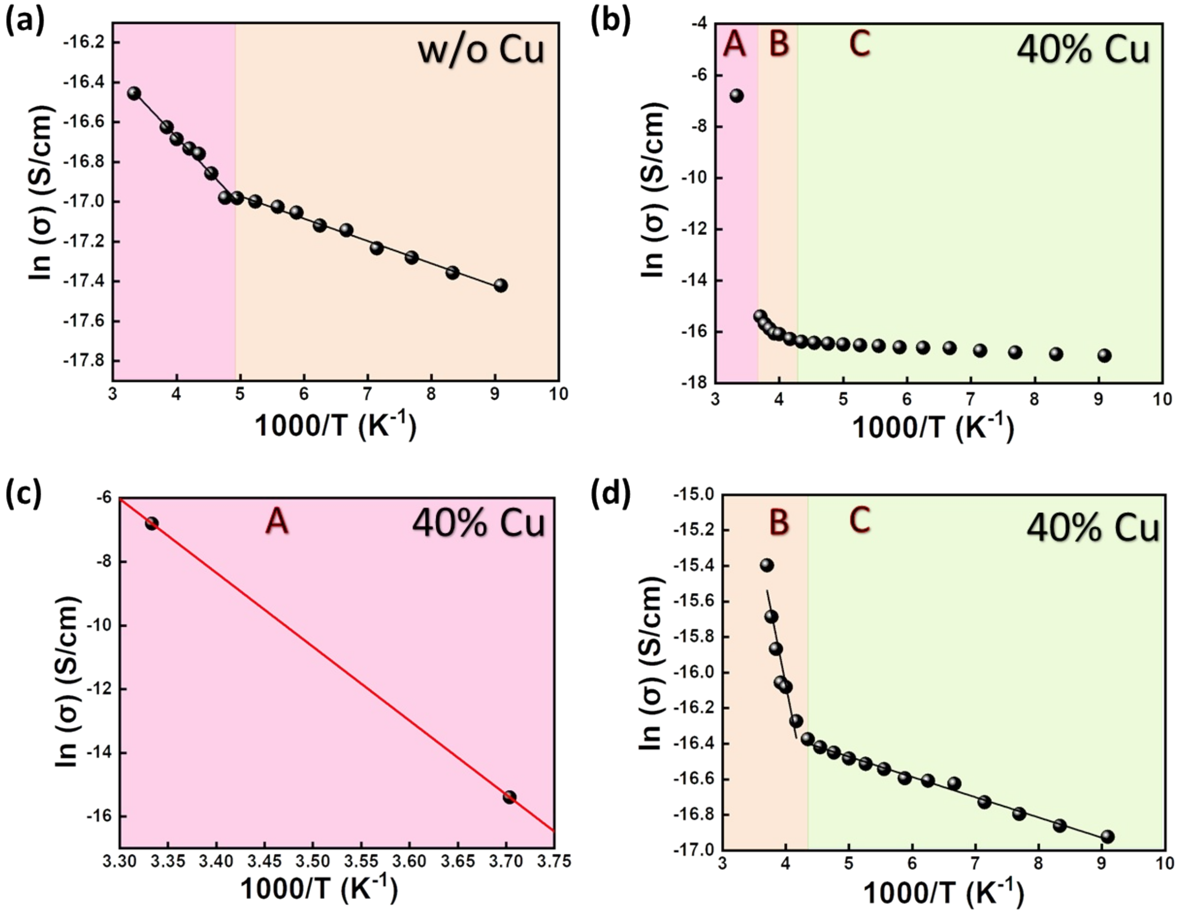

Fig. S12 Arrhenius plots for activation energy estimation: (a) Pristine $MAPbBr_3$ and (b) 40% Cu-$MAPbBr_3$. Zoom for region A (c) and regions B and C (d) for 40% Cu-$MAPbBr_3$.

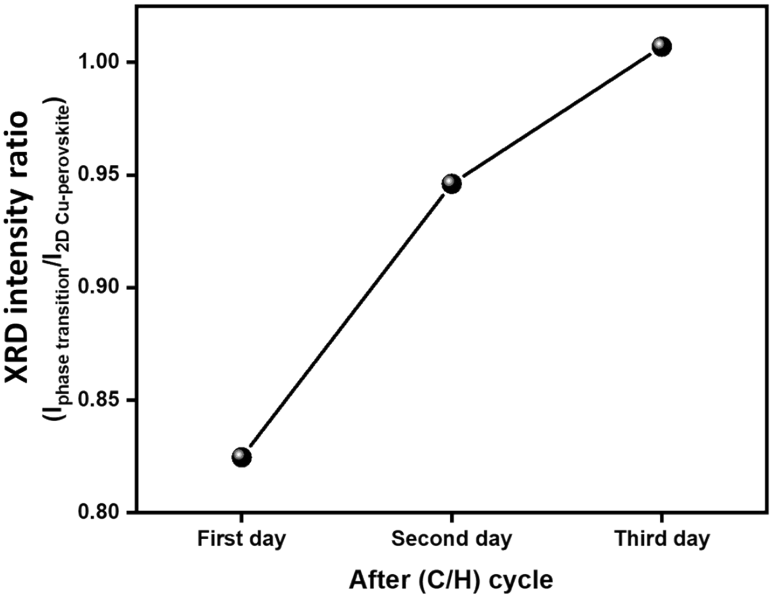

Fig. S13 Dependence of XRD peak (phase transition peak and MA_2CuBr_4 peak) intensity ratio on time.

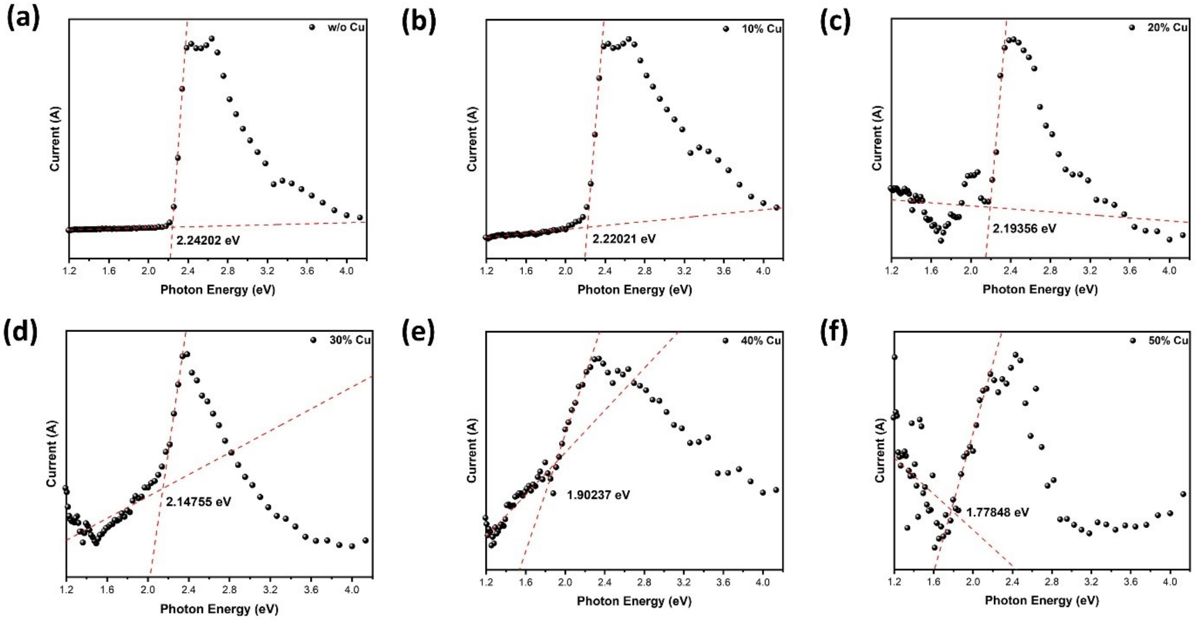

Fig. S14 Photocurrent spectra of pristine (a), 10% (b), 20% (c), 30% (d), 40% (e), and 50% (f) doped $MAPbBr_3$ at room temperature.

References

1 J. F. Janak, Proof that $\frac{\ensuremath{\partial}E}{\ensuremath{\partial}{n}_{i}}=\ensuremath{\epsilon}$ in density-functional theory, *Physical Review B*, 1978, **18**, 7165–7168.

2 Y. Li, S. Sanna and W. G. Schmidt, Modeling intrinsic defects in $LiNbO_3$ within the Slater-Janak transition state model, *The Journal of Chemical Physics*, 2014, **140**, 234113.

3 F. Bertoldo, S. Ali, S. Manti and K. S. Thygesen, Quantum point defects in 2D materials - the QPOD database. npj Comput Mater, 2022, **8**, 56.